International Journal of Mechanical Sciences 107 (2016) 136–149

Contents lists available at ScienceDirect

International Journal of Mechanical Sciences

journal homepage: www.elsevier.com/locate/ijmecsci

Material constitutive model and chip separation criterion influence on the modeling of Ti6Al4V machining with experimental validation in strictly orthogonal cutting condition

F. Ducobu *, E. Rivière-Lorphèvre, E. Filippi

University of Mons (UMONS), Faculty of Engineering (FPMs), Machine Design and Production Engineering Lab, 20 Place du Parc, B-7000 Mons, Belgium

ARTICLE INFO

Article history:
Received 11 July 2015
Received in revised form
3 December 2015
Accepted 5 January 2016
Available online 13 January 2016

Keywords:
Benchmark
Chip formation
Experiments
Finite element
Orthogonal cutting
Titanium alloy Ti6Al4V

ABSTRACT

The titanium alloy Ti6Al4V, although widely used in machining, is a hard-to-machine material, particularly due to the production of saw-toothed (or segmented) chips. The phenomena leading to this kind of chips are still an ongoing problem in the current literature, as well experimentally as numerically. An experimental orthogonal cutting setup on a milling machine is presented as a benchmark to validate finite element models. Its ease of implementation and near-to-zero cost should enable it to be used for any material, as long as the cutting speed is achievable by the feed rate of the machine. In addition to the study of chip formation, this setup could also allow to carry out long, although interrupted, machining tests to analyze tool wear. A numerical finite element model is then introduced to model the chip formation in the same cutting conditions. The comparison of the numerical results with the experiments shows that the level of the forces is mainly influenced by the material constitutive model, while the chip morphology is mostly impacted by the chip separation criterion. Either experimentally or numerically, the mechanism leading to the formation of a Ti6Al4V saw-toothed chip, for the cutting conditions of this study, is the conjunction of the adiabatic shear band in the primary shear zone, followed by the propagation of a crack into it.

1. Introduction

Ti6Al4V is the most widely used titanium alloy, according to [1–4]. It is mainly composed of 6% of aluminum and 4% of vanadium in mass, explaining its name. At room temperature, Ti6Al4V is an $\alpha + \beta$ alloy (90% in volume of the α phase [5]). Saw-toothed chips (in the literature, this type of chips is also called segmented, serrated or fragmented) are common in Ti6Al4V machining. This kind of chips can often lead to tool vibration and wear problems [6] but can sometimes facilitate chip fragmentation. It should therefore be avoided, or, at least, the size of the teeth should be reduced to decrease these problems. The comprehension of the mechanisms leading to this type of chips would improve Ti6Al4V machinability.

Three main theories explain the formation of Ti6Al4V saw-toothed chips [7]. The first one is the adiabatic shear band [8–12], in which large shear in the primary shear zone leads to thermal and strain softening of the material. The crack propagation [13,14], secondly, in which a continuous crack appears at the free surface of the chip and propagates towards the tool due to the large shear in the primary shear zone. Thirdly, the combination of the two previous theories in which the adiabatic shear band is the precursor of the material failure and the crack propagation [9,15,16]. The formation mechanisms of this kind of chips are also studied for other materials such as hardened steels [24,25] or aluminium alloys [25] at cutting speeds higher than for Ti6Al4V. Experimental (quick-stop) orthogonal cutting studies on these materials show that the formation of a saw-toothed chip is performed through the mechanisms of the third theory [24,25]. In the case of hardened steels, ductile fracture is observed under severe cutting conditions; large plastic strains occur otherwise [24]. Cutting speed, uncut chip thickness and hardness are the dominant parameters to control the saw-toothed chip formation [24,25].

Different finite element models can be found in the literature to form saw-toothed Ti6Al4V chips. Some of them are developed with Deform-2D, either with [17] or without [18,19] damage properties for the machined material. They lead to a chip with less angular, more rounded teeth than for the experimental chip. This could be due to the remeshing and/or a too coarse mesh. These models consider that the formation of the saw-toothed chip is due to the adiabatic shear band. Calamaz et al. [16] present a numerical chip produced with Forge 2005, with and without damage. The

* Corresponding author. Tel.: +32 65 45 47; fax: +32 65 45 45.
E-mail address: Francois.Ducobu@umons.ac.be (F. Ducobu).

http://dx.doi.org/10.1016/j.ijmecsci.2016.01.008
0020-7403/

chip morphology with damage (therefore formed due to the conjunction of the adiabatic shear band and the crack propagation) is closer to their experimental reference. Mabrouki et al. [20] and Zhang et al. [21,22] developed Lagrangian models with Abaqus without remeshing but with damage and using a sacrificial layer. This layer is of the same order of magnitude as the cutting edge radius of the tool and they add a chamfer to the workpiece to limit the deformation of the finite elements in that zone. Such models with a sacrificial layer are therefore developed for a defined set of cutting conditions. Their modification implies to adapt the geometry of the model (at least).

In the recent literature [7,23], numerically as well as experimentally, the theory coupling the adiabatic shear band and the crack propagation (third theory) competes with the adiabatic shear band theory (first theory). The mechanisms leading to the formation of a Ti6Al4V saw-toothed chip are consequently an ongoing problem in the literature.

An orthogonal cutting finite element model developed with Abaqus and relying on the third theory [7] is presented in this paper to form a numerical Ti6Al4V saw-toothed chip. This model is intended to handle various cutting conditions (in terms of cutting speeds and depths of cut) without the need to modify it. Following the development of a numerical model, its validation with an experimental reference [26] is needed. This kind of validation usually mainly concentrates on the chip formation, the chip morphology and the cutting forces. During the development of a numerical model of orthogonal cutting, such a reference with the complete information on all the parameters and the results is almost always missing in the literature, regardless of the machined material. Moreover, as numerical simulations model the simplified case of orthogonal cutting, the validation experiments should also be carried out in this cutting configuration. Usually, to get as close as possible to the assumptions of orthogonal cutting, two alternatives are considered in turning [26]: Altintas [27] performs face turning of the end of a tube with a large diameter and a small thickness (the width of the tool is larger than the thickness of the tube), while Mahnama and Movahhedy [28] carry out plunge turning of large diameter radial grooves having a width smaller than that of the tool. The second method is often used because it allows to perform one experiment per groove and thus several tests on a single part. However, the radius of the sample influences the cutting due to the curvature of the surface to machine. This takes importance when the depth of cut decreases. It cannot be neglected anymore for small depths of cut (or the radius of the sample should increase dramatically) and the process moves away from orthogonal conditions. Having experimental results in the same cutting conditions and configuration as the modeling is crucial for its validation, what is more knowing the large amount of constitutive models available in the literature, even for a single material, and leading to potentially very different results [29].

To fill this gap, this paper presents a simple setup to perform orthogonal cutting experiments on a standard milling machine [26] in order to constitute a benchmark aiming at the validation of finite element models. The geometry of the sample is chosen to reduce the volume of material as well as the machining costs. The results of the finite element model can then be compared to the experiments for the cutting conditions leading to a saw-toothed chip. This experimental reference is then used to improve the numerical results and highlight the influence of the material constitutive model and the chip separation criterion. The results of the numerical model are finally compared to the other cutting conditions adopted in the experiments.

2. Experimental Ti6Al4V chip formation

2.1. Orthogonal cutting setup

The Ti6Al4V alloy used for the experiments is annealed (at 750 °C during an hour followed by air cooling) Ti6Al4V grade 5 (AMS 4928). Its main properties and detailed composition according to AMS 4928 standard are available in [30].

A five-axis high speed milling machine Deckel-Maho DMU-80T is used as a planning machine to remove a layer of material of variable, but larger than the tool edge radius, thickness [26]. In this configuration (Fig. 1), the cutting movement is an horizontal displacement generated by the sample (inserted into the spindle) with respect to the stationary tool (fixed on the machine table), ensuring that the cutting is really orthogonal. This setup could also allow to carry out long (interrupted) machining tests to analyze tool wear but this is not the goal of this study. Dry cutting conditions are adopted.

The sample (Fig. 2) is an 18 mm diameter cylinder with three parallel tenons of 1 mm wide, 10 mm long and 2 mm high. The flatness deviation of the tenons is lower than 5 μm and their arithmetic roughness is equal to $R_a = 0.2$ μm. The width of the tenons is reduced to 1 mm to minimize the efforts in the spindle bearings and to give the forces value per mm width as in 2D plane strain numerical models [16,31–33]. The plane strain hypothesis requires a ratio of the width of cut on the depth of cut (i.e. the undeformed chip thickness) larger than 3.5. It is satisfied for all the depths of cut adopted in this paper (the larger is 280 μm).

The cutting speed, i.e. the feed rate of the machine, is set to the maximum achievable value by the DMU-80T, 30 m/min. This value is in the range recommended by the tool manufacturer SECO for

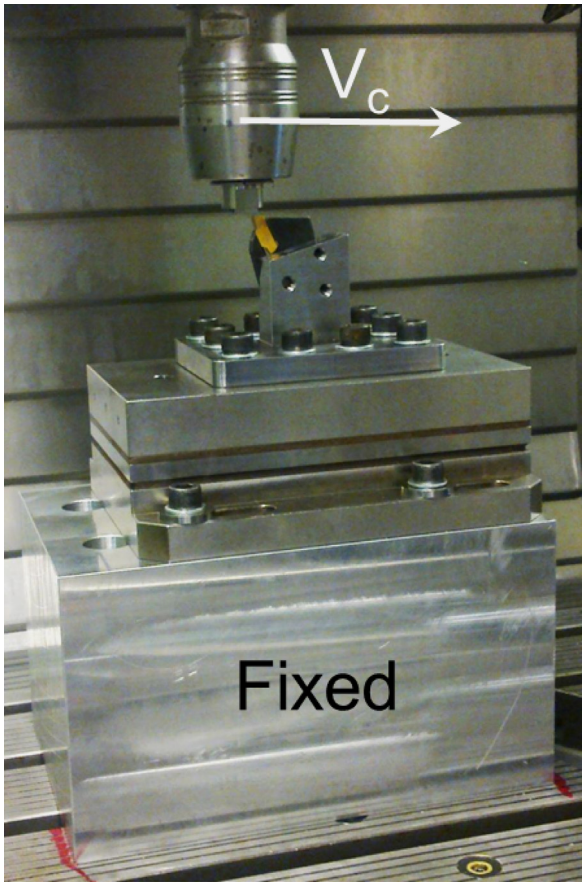

Fig. 1. Cutting configuration on the milling machine [26].

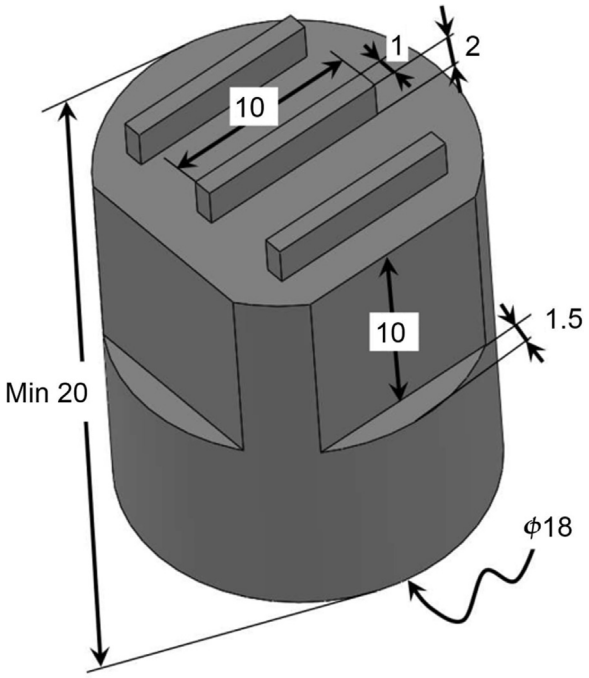

Fig. 2. Sample geometry, with dimensions in mm [26].

Table 1
Cutting conditions of the experiments.

Cutting speed (m/min)	30
Depths of cut (μm)	40, 60, 100, 280
Width of cut (mm)	1
Length of cut (mm)	10
Rake angle (deg)	15
Clearance angle (deg)	2
Cutting edge radius (μm)	20

the standard version of the tool and Ti6Al4V (27–39 m/min) [34]. In order to confirm that the desired cutting speed is reached, a Photron FASTCAM SA3 high speed camera has been used to count the number of frames during the cut at an acquisition frequency of 30,000 frames/s. It results in a difference with the theoretical speed of 1% (29.65 m/min with a standard deviation of 0.09 m/min) [26], which allows to certify that the cut is performed at the requested speed.

The tool is placed on the machine table through an interface part fixed on the force sensor. This tool is custom made by SECO from standard element (LCGN160602-0600-GX-X, CP500) to machine radial grooves by turning [34] in order to provide a rake angle of 15°, a clearance angle 2° and a cutting edge radius 20 μm, as in the experiments of Sun et al. [35] and the numerical model introduced in [7].

Each cutting test takes 0.02 s, the time required to travel the 10 mm length of the tenon at 30 m/min. Four values of the depth of cut, h, are adopted: 280 μm, 100 μm, 60 μm and 40 μm, while the cutting speed is kept constant. The cutting conditions of the experimental tests are summarized in Table 1; each cutting condition was repeated 3 times. The cutting forces are measured in the three directions with a Kistler 9257B dynamometer at the sampling frequency of 70 kHz. The rest of the acquisition chain is composed of the multichannel charge amplifier Kistler 5070A, the data acquisition system (DAQ) Kistler 5697A2 and the DynoWare software.

2.2. Results

2.2.1. Chips morphology

The chips were observed with an optical microscope [26]. They were embedded into epoxy resin to stand on their edge before being polished straight across their length. They were then etched during about 45 s by Kroll's reagent to reveal the Ti6Al4V microstructure by coloring the β phase in dark brown (the darker color on black and white microscope views provided in this paper).

The chip for the depth of cut of 280 μm is saw-toothed and its teeth seem globally to be similar (Fig. 3(a), magnification factor of 50). Fig. 3(b)–(d) presents the three other chips at a magnification factor of 200. They are quasi-continuous chips although the one at 40 μm has very small and irregular teeth along its entire length. Thanks to the small cutting length (10 mm), the chips are short and not rolled up. This prevents them to be deformed during the unrolling preceding the embedding. No error from that operation arises allowing to directly compare experimental and numerical values.

The saw-toothed chip is now analyzed more in detail. Such a chip is usually characterized by its undeformed tooth length, L, its tooth height, H, and its valley, C, highlighted in Fig. 4. The mean and standard deviation values of these three lengths are presented in Table 2 for 25 teeth. The standard deviation is similar (and small) for each length, except for the valley (C) which has a standard deviation larger than 10% of its mean value.

With a higher magnification factor (Fig. 5), it is clearly observed that the grains are highly deformed in the primary shear zone but not inside the teeth. Crack propagation characteristics are noticed on the teeth flanks: the grains are almost not deformed and the surfaces are irregular. A crack propagates therefore inside the primary shear zone, from the free surface of the chip to the tool.

These observations allow to take position relative to the different theories about the Ti6Al4V saw-toothed chip formation available in the literature. At a cutting speed of 30 m/min, a depth of cut of 280 μm and for the tool considered, the formation of the saw-toothed chip is due to deformation and crack propagation inside the primary shear zone.

2.2.2. Cutting forces

The average value of the force in the direction perpendicular to the cutting plane is close to zero, confirming that the cut is orthogonal and not oblique [26]. As expected for a saw-toothed chip, the temporal evolution of the efforts during a test at the depth of cut of 280 μm exhibits variations at a high frequency and with large amplitudes, as shown in Fig. 6.

At the three other depths of cut (100 μm, 60 μm and 40 μm), the chip is quasi-continuous and therefore the forces are nearly constant and present smaller variations. As an illustration, they are plotted for the depth of cut of 60 μm in Fig. 7. A higher level of the forces is observed at the beginning of the test. It is due to the entrance of the tool in the workpiece which is similar to an impact on the tool.

Table 3 summarizes the average root mean square (RMS) values of the forces for each cutting condition. The values presented are averaged on three measurements for each depth of cut. As expected, the lower the depth of cut, the lower the level of the forces. It is interesting to note the growing influence of the tool edge radius on the cutting process: the ratio of the mean RMS values ($\frac{FF}{CF}$) increases, showing that the feed force decreases less quickly than the cutting force with the depth of cut.

2.2.3. Teeth formation frequency

For the saw-toothed chip geometry, the teeth formation frequency has been estimated through four methods [26]: the chip geometry, the Fast Fourier Transform (FFT) of the cutting force

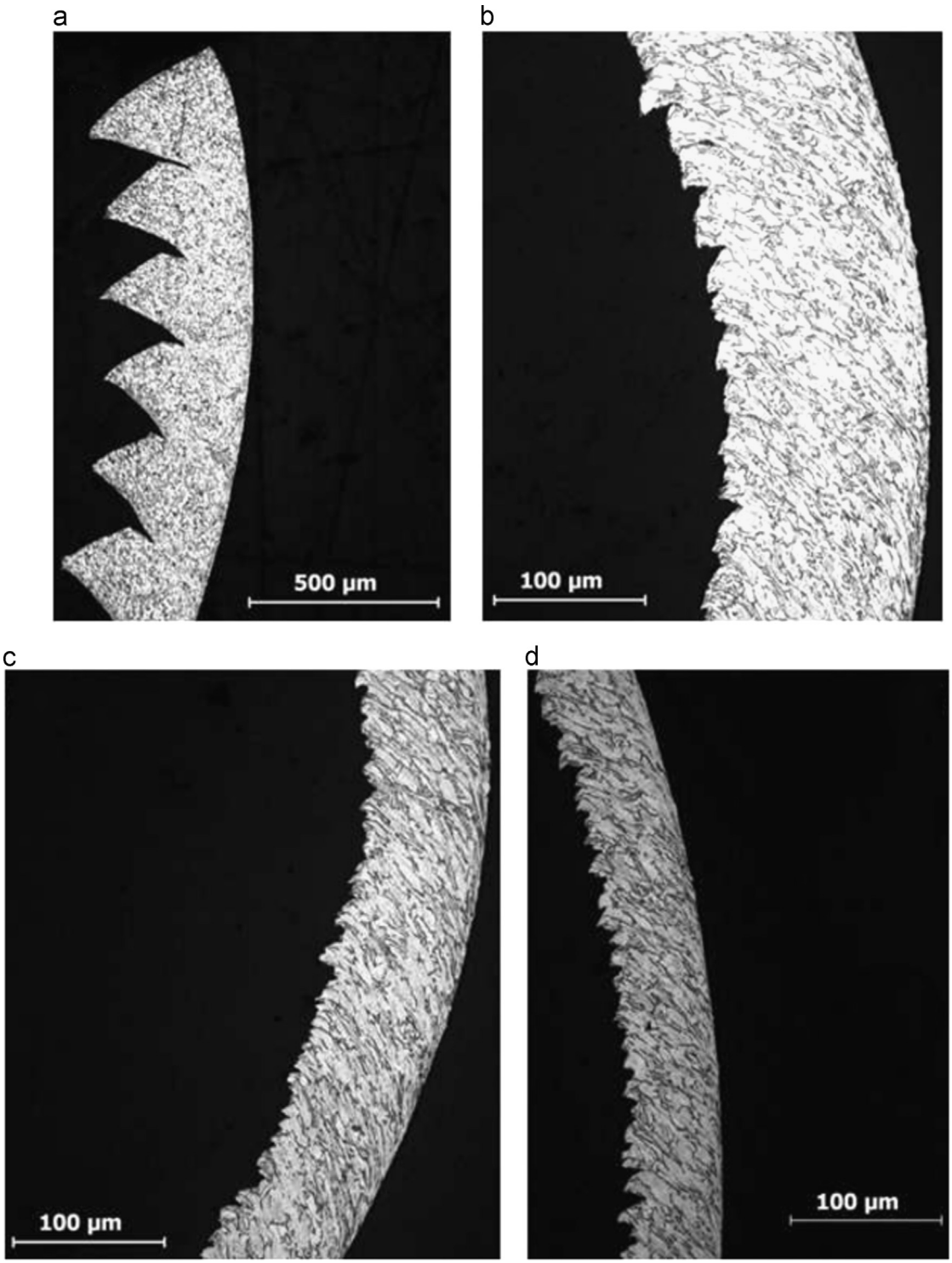

Fig. 3. Chips on optical microscope (a) 280 µm, (b)100 µm, (c) 60 µm and (d) 40 µm [26].

signal, the best sine in a least squares way fitted on the cutting force evolution and the machined surface roughness.

For the chip geometry, the teeth formation frequency is estimated from the undeformed tooth length, L, measured on 25 teeth (cf. Table 2) and the cutting speed, V_c (30 m/min) [35]:

$$F_g = \frac{V_c}{L} \tag{1}$$

The frequency resulting of an undeformed tooth length of 206 µm (Table 2) is 2427 Hz with a standard deviation of 200 Hz.

For the FFT of the cutting force signal, standard precautions were taken to limit the phenomena of aliasing and leakage, particularly through the introduction of a Hanning filter. The mean value of the frequency with this method, f_f, is 2038 Hz with a standard deviation of 834 Hz, which is quite high. This dispersion can be explained by the numerous high peaks under 5 kHz, making it hard to find the one corresponding to the formation frequency. For the best sine in a least squares way fitted on the cutting force evolution, the average formation frequency, f_s, is 2032 Hz with a standard deviation of 832 Hz, values very close to

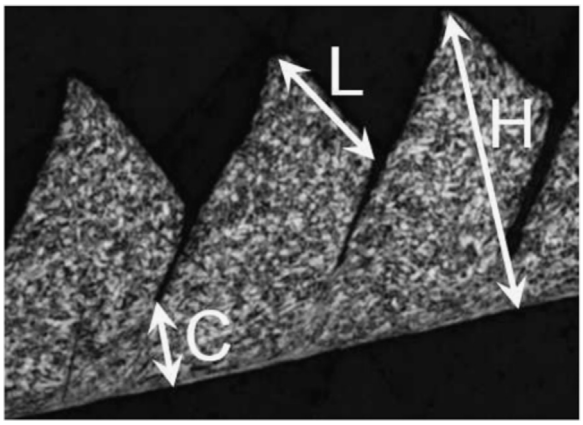

Fig. 4. Characteristic lengths of a typical saw-toothed chip.

Table 2
Characteristic lengths of the saw-toothed chip at 280 μm for 25 teeth (σ_x: standard deviation of the length x) [26].

Indicator	L	H	C
x (μm)	206	288	157
σ_x (μm)	17	14	21

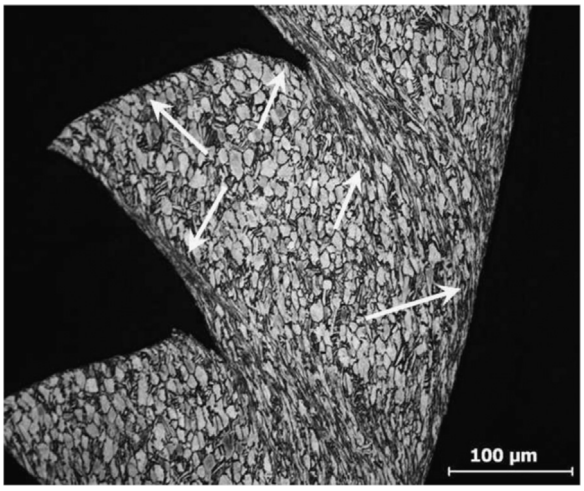

Fig. 5. Chip microstructure for the chip at 280 μm (arrows point to the different zones of a tooth with grains deformation of different intensities) [26].

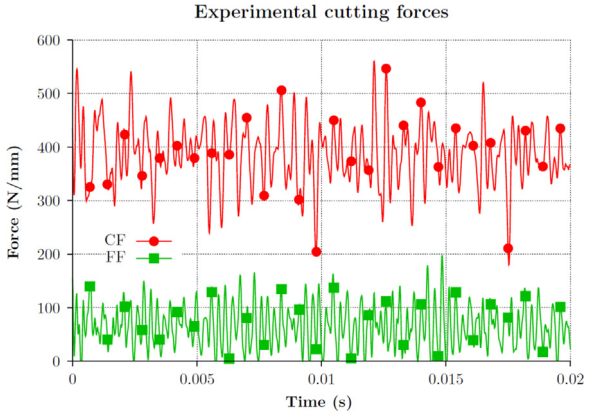

Fig. 6. Cutting forces (cutting force, CF, and feed force, FF) for a cutting speed of 30 m/min and a depth of cut of 280 μm [26].

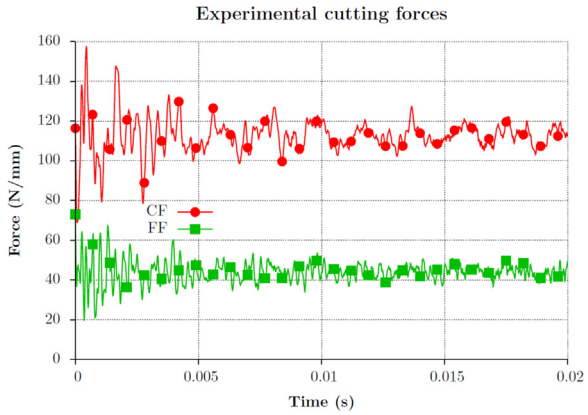

Fig. 7. Cutting forces (cutting force, CF, and feed force, FF) for a cutting speed of 30 m/min and a depth of cut of 60 μm [26].

Table 3
Experimental cutting forces summary (3 repetitions at each depth of cut) [26].

h (μm)	RMS CF (N/mm)	RMS FF (N/mm)	$\frac{FF}{CF}$
280	386 ± 1	76 ± 7	0.20
100	172 ± 2	50 ± 1	0.29
60	111 ± 2	44 ± 1	0.40
40	86 ± 2	41 ± 1	0.47

those obtained by the FFT method. For the last method, the FFT of the roughness profile of the machined surface is performed as it has a cyclic evolution close to that of the cutting force [26]. The mean teeth formation frequency of the measured profiles is 2082 Hz with a standard deviation of 52 Hz. This formation frequency is very close to the two previous ones but the standard deviation is much lower.

2.3. Conclusions of the experiments

Ti6Al4V strictly orthogonal cutting experiments were performed on a high speed milling machine to constitute a benchmark for numerical modeling. The forces were measured and the chips observed with an optical microscope. Two types of chip morphology were obtained: quasi-continuous at 100 μm, 60 μm and 40 μm (with small teeth for this depth of cut) and saw-toothed at 280 μm. The observations on optical microscope showed that, for the cutting conditions adopted in this paper, the formation mechanism of a Ti6Al4V saw-toothed chip resulted of the high deformations and the crack propagation inside the primary shear zone. The forces were measured and decreased with the depth of cut. They were cyclic for the saw-toothed chip and nearly constant for the quasi-continuous ones, as expected. The teeth formation frequency of the saw-toothed chip was approximately 2100 Hz (with the lowest standard deviation for the roughness method).

3. Finite element model presentation

A finite element model has been developed with the commercial software ABAQUS/Explicit v6.11 in order to study numerically the Ti6Al4V chip formation [7]. It is a 2D plane strain orthogonal cutting model taking into account the area close to the cutting edge of the tool. It was developed with the constraint to respect the physical phenomena and not influence the chip formation (with a predefined chip separation line, for example [20]) [7]. The tool geometry and the cutting conditions are the same as

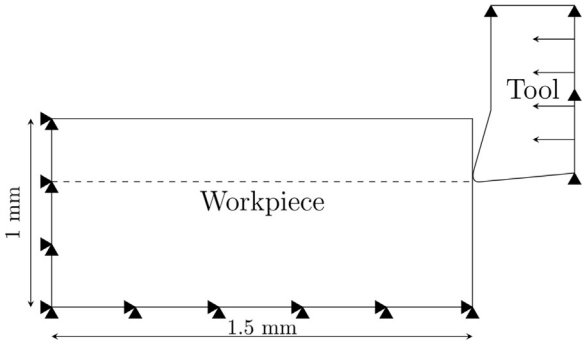

Fig. 8. Initial geometry and boundary conditions of the model.

for the experimental study: the rake angle is 15°, the clearance angle is 2° and the cutting edge radius is 20 µm. The cutting speed is set to 30 m/min and the depth of cut takes four values: 280 µm, 100 µm, 60 µm and 40µm. The workpiece is modeled as a rectangular block of 1.5 mm long and 1 mm wide and is fixed in space (Fig. 8).

The behavior of Ti6Al4V is described by the Hyperbolic TANgent (TANH) model introduced by Calamaz et al. [16]. It consists of an upgraded Johnson–Cook model [36] to take strain softening into account, which would be one of the causes for the formation of saw-toothed Ti6Al4V chips. This strain softening phenomenon would occur at strains larger than 0.5, most likely due to dynamic recrystallization (mainly in the β phase field), according to Ding et al. [37]. In the recent literature, an increasing number of authors [7,16,19] recommend to use the TANH model instead of the Johnson–Cook model in finite element modeling, regardless of the finite element software, to form saw-toothed Ti6Al4V chips.

The TANH equation is expressed as follows [16]:

$$\sigma = \left[A + B\,\varepsilon^{n}\left(\frac{1}{\exp(\varepsilon^{a})}\right)\right]\left[1 + C\ln\frac{\dot{\varepsilon}}{\dot{\varepsilon}_0}\right]\left[1-\left(\frac{T-T_{room}}{T_{melt}-T_{room}}\right)^{m}\right]\left[D+(1-D)\tanh\left(\frac{1}{(\varepsilon+S)^{c}}\right)\right] \quad (2)$$

with

$$D = 1-\left(\frac{T}{T_{melt}}\right)^{d} \quad \text{and} \quad S = \left(\frac{T}{T_{melt}}\right)^{b}$$

Parameters A, B, C, m and n are material properties having the same meaning as for Johnson–Cook model, while a, b, c and d are the new constants introduced by the TANH model, T_{melt} is the melting temperature, T_{room} is the room temperature, ε is the plastic strain and $\dot{\varepsilon}_0$ is the reference strain rate. Their values are given in Table 4.

The Ti6Al4V metallurgical state for which Calamaz et al. [16] identified the TANH model is not known. It could therefore be different of the annealed Ti6Al4V used for the experiments presented in the first part of this paper. These parameters are consequently considered as first values that could be modified for the TANH model to better fit the Ti6Al4V used. The tool material is tungsten carbide and its behavior is described by a linear elastic model. The material properties of Ti6Al4V and tungsten carbide adopted in the numerical model can be found in Table 4.

Coulomb's friction, with a low coefficient value (0.05) [7], is used to model friction at the tool–chip interface and all the friction energy is converted into heat, which is usually assumed [40]. This heat flux is then allocated to the workpiece and the tool via the β coefficient modeling the fraction of this heat flux going into the workpiece. The sharing of this flux is often carried out equally between the two parts in contact (and thus $\beta = 0.5$). More rigorously, this coefficient is calculated with the effusivities of the workpiece and the tool [40]:

$$\beta = \frac{E_{wp}}{E_{wp}+E_t} \quad (3)$$

with E_{wp} and E_t the effusivity of, respectively, the workpiece and the tool. The effusivity is expressed by

$$E = \sqrt{k\rho c_p} \quad (4)$$

In the case of the tungsten carbide–Ti6Al4V couple, $\beta \approx 0.25$. This value is adopted in the model, meaning that about 25% of the heat generated at the interface between the tool and the workpiece go into the part. Only conduction is considered and all the part faces are adiabatic. The transformation of the deformation to heat is assumed to occur with an efficiency of 90% [38,40,41].

Explicit Lagrangian formulation is adopted and a chip separation criterion must therefore be introduced in the model. The chip separation criterion consists of an "eroding" elements method with crack propagation in the workpiece. The criterion uses the temperature dependent tensile failure of Ti6Al4V [30], as previously presented in [7]. When the limit value of the stress is reached in a finite element, this element is removed from the visualization, all of its stress components are put to zero and its rigidity is reduced at 1% of undamaged Ti6Al4V. The suppression of an element introduces a crack in the workpiece and allows the chip to come off. Fig. 9 shows the evolution of the tensile failure of Ti6Al4V versus temperature introduced in the model.

Table 4
Material properties and cutting conditions of the numerical model [16,30,38,39].

TANH model	A (MPa)	968
	B (MPa)	380
	C	0.02
	m	0.577
	n	0.421
	T_{room} (K)	298
	T_{melt} (K)	1878
	a	1.6
	b	0.4
	c	6
	d	1
Inelastic heat fraction	Ti6Al4V	0.9
Density, ρ (kg/m^3)	Ti6Al4V	4430
	Carbide	15,000
Young's modulus, E (GPa)	Ti6Al4V	113.8
	Carbide	800
Expansion, α (K^{-1})	Ti6Al4V	8.6e^{-6}
	Carbide	4.7e^{-6}
Conductivity, k (W/mK)	Ti6Al4V	7.3
	Carbide	46
Specific heat, c_p (J/kg K)	Ti6Al4V	580
	Carbide	203
Friction coefficient		0.05
Friction energy to heat (%)		100
Heat partition to part (%)		25
Cutting speed (m/min)		30
Depths of cut (µm)	40, 60, 100, 280	
Rake angle (deg)		15
Clearance angle (deg)		2
Cutting edge radius (µm)		20

4. Comparison with the experiments at 280 µm

The comparison between the modeling and the experiments will firstly only be performed for the depth of cut of 280 µm as it results in a saw-toothed chip, a type of chip harder to model than a continuous chip. The three other ones will be included later in the comparison (cf. Section 7).

4.1. Discussion

Fig. 10 presents the comparison between the numerical and the experimental chips. They are both saw-toothed and their morphologies are qualitatively close to each other. However, numerical teeth are deeper (they have smaller valleys and lengths, see Table 5) and the second and third teeth contain a crack (so long in the third tooth that it is broken). It is noted that the chip curl is different: the numerical one is larger. This is due to the smaller valleys leading to a less stiff chip. The first tooth, whatever numerical or experimental, will not be taken into account in the comparison as the cutting regime is not yet established.

As for the experiments, the undeformed tooth length, L, the tooth height, H, and the valley, C, (Fig. 4) were measured on the modeled chip. These three lengths are smaller for the numerical chip than the experimental one (Table 5), in accordance with the observations in Fig. 10. It is therefore deduced that the teeth deformation is not sufficient (lower tooth length) and the crack propagates too easily (lower valley) in the formation mechanism of the modeled chip.

In the modeling, high shear and temperature increase occur in the very narrow primary shear zone during the chip formation as well as crack propagation. It starts at the free chip surface and propagates towards the tool. This chip formation mechanism is very close to the one observed experimentally. This indicates that, except for the crack growing too deep in the primary shear zone, the numerical model takes correctly into account the physical phenomena occurring during the saw-toothed chip formation of Ti6Al4V in orthogonal cutting.

Fig. 11 presents the evolutions of the cutting forces versus time. Numerical and experimental are both cyclic, which was expected as both chips are saw-toothed for these cutting conditions. For the numerical one, five maxima are identified and are linked to the

Table 5
Summary of the characteristic lengths of the saw-toothed chips at 280 μm (experiments: 25 teeth, simulation: 4 teeth, σ_x: standard deviation of the length x).

Case	L (μm)	σ_L (μm)	C (μm)	σ_C (μm)	H (μm)	σ_H (μm)
Exp.	206	17	157	21	288	14
Sim.	162	7	72	13	292	4

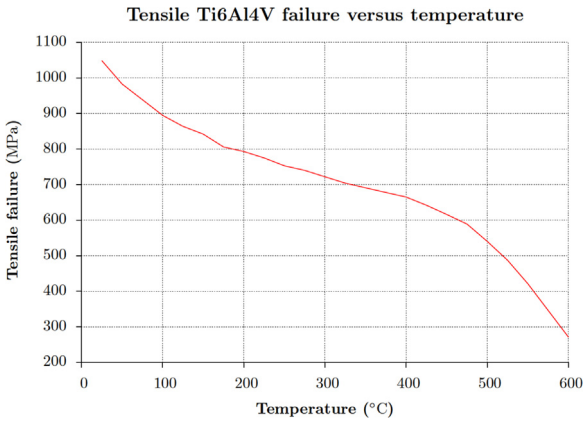

Fig. 9. Tensile Ti6Al4V failure evolution versus time [30].

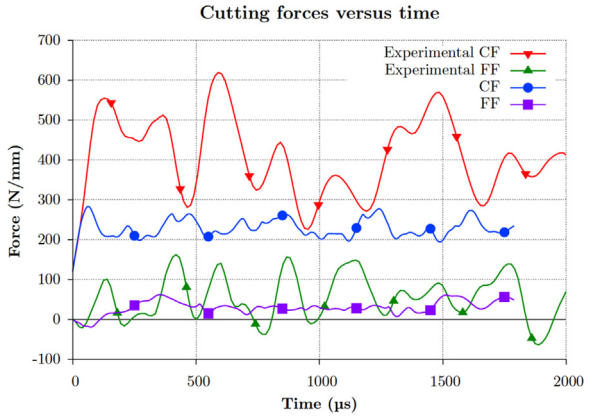

Fig. 11. Comparison of the cutting forces (cutting force, CF, and feed force, FF) for the initial model at a cutting speed of 30 m/min and a depth of cut of 280 μm, low-pass filter cutoff frequency at 10 kHz.

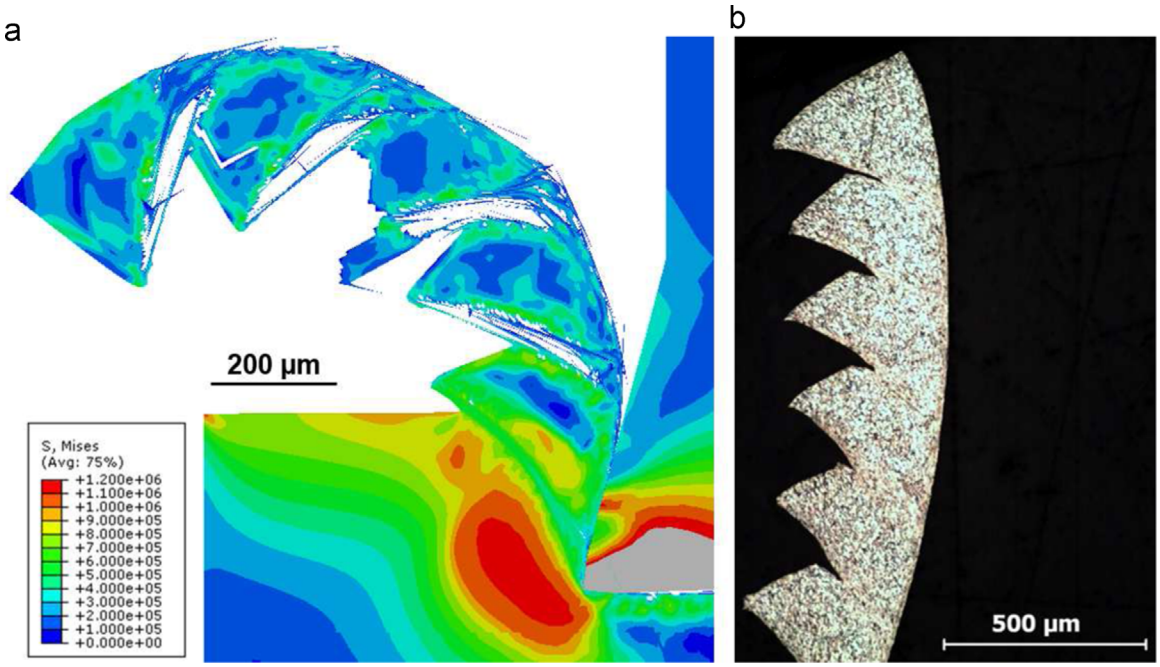

Fig. 10. Chip morphologies at a depth of cut of 280 μm (a) numerical (Von Mises stresses contours (e^3 Pa)); (b) experimental.

Table 6
RMS cutting forces and teeth formation frequencies comparison.

Case	CF (N/mm)	FF (N/mm)	f_g (Hz)	f_f (Hz)	f_s (Hz)
Exp.	386	76	2427	2038	2032
Sim.	231	72	3086	2436	2604

formation of the five teeth shown in Fig. 10(a). A significant difference is noted between the level of the forces: it is higher for the experimental one, as well as the magnitudes of the forces' variations. These observations are confirmed by the RMS values summarized in Table 6: the numerical cutting force is 40% lower than the experimental reference value.

As the machined surface roughness method is not suitable for a numerical model, the teeth formation frequency is evaluated with the three remaining methods: the chip geometry, the FFT of the cutting force signal and the best sine in a least squares way fitted on the cutting force evolution. Table 6 compares the values obtained with these of the experiments. It appears that the numerical frequency is always larger than the experimental one (it is of the order of 2700 Hz versus of the order of 2100 Hz). This is explained by the shorter teeth for the modeled chip, which leads to a higher frequency. They are, however, of the same order of magnitude, indicating that the model represents accurately the dynamics of the phenomena.

4.2. Conclusions of the comparison

The numerical model gave results qualitatively close to the experiments. Both chips were saw-toothed and formed with very similar mechanisms: deformation in the primary shear zone, followed by a crack propagation. The teeth of the numerical chip had a smaller valley and some of them contained a crack. It is deduced that the crack propagation is too important in the modeling by comparison with the experiments. The teeth formation frequency was evaluated in both cases. It turned out that the numerical frequency was higher than the experimental one. The teeth being shorter for the modeled chip, it was expected.

The most significant difference in the comparison was the level of the cutting force, largely underestimated by the model. Both cutting forces had a cyclic evolution, which was expected given the chip morphology. The RMS value and the magnitude of the variations of the numerical cutting force were smaller than that of the experiments. The parameters of the TANH model are directly linked to the level of the forces. As announced in the model presentation (cf. Section 3), the metallurgical state of Ti6Al4V for which the TANH parameters have been identified is unknown. When analyzing the results, it becomes very likely that they do not correspond to the Ti6Al4V used in the experiments. It is therefore proposed to adapt the constitutive model to better represent the machined material and consequently bring the cutting forces closer to each other.

5. Influence of the material constitutive model on the results

5.1. Material constitutive model modifications

Numerous models can be found in the literature to model the Ti6Al4V behavior during machining. The Johnson–Cook (J–C) model [36] is the most used so far:

$$\sigma = \left[A + B\,\varepsilon^{n}\right]\left[1 + C\ln\frac{\dot{\varepsilon}}{\dot{\varepsilon}_0}\right]\left[1 - \left(\frac{T - T_{room}}{T_{melt} - T_{room}}\right)^{m}\right] \tag{5}$$

The set of parameters adopted is given in Table 7. As presented earlier in Section 3, the strain softening should be taken into account when modeling the Ti6Al4V machining. In the recent literature and in addition to the TANH model already presented, mainly three models exhibit strain softening.

Table 7
Parameters of the constitutive models [19,42–44].

J–C model			
A (MPa)		862.5	
B (MPa)		331.2	
C		0.012	
m		0.8	
n		0.34	
Modified J–C model			
A (MPa)	968	f	0.11
B (MPa)	380		
C	0.0197		
m	0.577		
n	0.421		
Karpat model			
E (MPa)	1215	n	0.06033
F (K^{-2})	$-2.81e^{-8}$	p	0
G (K^{-1})	$-7.694e^{-4}$	q	0.015
H	1.5815	r	1
L	6	s	7
M	0.6		
Sima model			
A (MPa)	724.7	g	2
B (MPa)	683.1	h	5
C	0.035	k	1
m	1	l	1
n	0.47	u	0.05

The first flow stress model is the modified Johnson–Cook, a second modification of the J–C model by Calamaz et al. [43]. In this model, the magnitude of the strain softening is controlled by parameter f (Table 7):

$$\sigma = \left[A + B\left(\frac{1}{\dot{\varepsilon}}\right)^{f}\varepsilon^{(n-0{,}12\ (\varepsilon\dot{\varepsilon})^{f})}\right]\left[1 + C\ln\frac{\dot{\varepsilon}}{\dot{\varepsilon}_0}\right]\left[1 - \left(\frac{T - T_{room}}{T_{melt} - T_{room}}\right)^{m}\right] \tag{6}$$

The second constitutive model was introduced by Karpat [44] (Karpat model), again with a hyperbolic tangent function. The main difference by comparison with the TANH model of Calamaz et al. [16] is that it is possible not to have strain softening when the temperature is low:

$$\sigma = \left[E\,\varepsilon^{n}\right]\left[F\,T^{2} + G\,T + H\right]\left[1 - \left\{1 - \left(\frac{\ln\dot{\varepsilon}_0}{\ln\dot{\varepsilon}}\right)^{q}\right\}\frac{1}{L\tanh(\varepsilon)}\right]\left[M + (1 - M)\left\{\tanh\left(\frac{1}{(\varepsilon + p)^{r}}\right)\right\}^{s}\right] \tag{7}$$

The parameters of this model are provided in Table 7.

The third model is a modification of TANH by Sima and Özel [19] (Sima flow stress). It was introduced to provide a better control on the thermal softening [19]:

$$\sigma = \left[A + B\,\varepsilon^{n}\left(\frac{1}{\exp(\varepsilon^{g})}\right)\right]\left[1 + C\ln\frac{\dot{\varepsilon}}{\dot{\varepsilon}_0}\right]\left[1 - \left(\frac{T - T_{room}}{T_{melt} - T_{room}}\right)^{m}\right]\left[D + (1 - D)\left\{\tanh\left(\frac{1}{(\varepsilon + R)^{k}}\right)\right\}^{u}\right] \tag{8}$$

with

$$D = 1 - \left(\frac{T}{T_{melt}}\right)^{l} \quad \text{and} \quad R = \left(\frac{T}{T_{melt}}\right)^{h}$$

Fig. 12 presents the stress–strain evolutions of the constitutive models at fixed temperature and strain rate. The four models taking strain softening into account can be classified into two

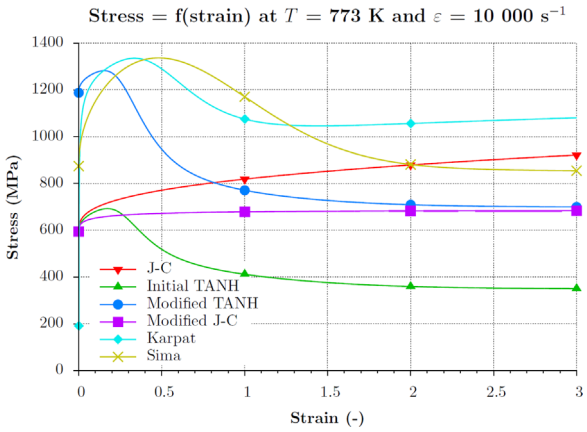

Fig. 12. Stress–strain evolutions at 773 K and 10,000 s^{-1}.

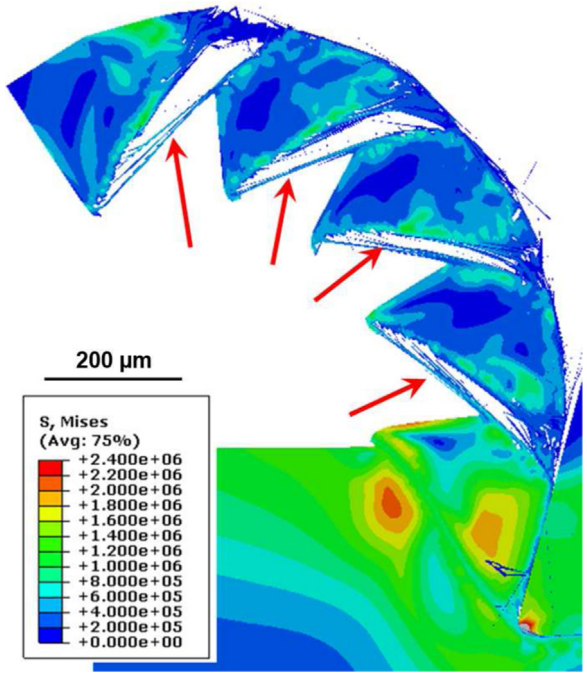

Fig. 13. Chip morphology (Von Mises stresses contours (e^3 Pa)) of the second model (arrows point to the elements linking two successive teeth).

groups according to the stress level: low for the TANH [16] and the modified Johnson–Cook [43] models and high for the Karpat [44] and the Sima [19] models. Karpat [44] and Sima [19] models lead to stresses nearly two times higher than for the TANH model at small strains. It is important to point out that this large difference in the stress level is significant although these four models are intended to describe the same material, Ti6Al4V. It could explain the difference on the forces observed in the modeling.

The stress level should therefore be pulled up while maintaining the TANH curve shape, and the strain softening in particular. This is achieved by acting on the A parameter in the TANH model (cf. Eq. (2)). In order to bring the TANH curve to the level of Karpat's [44] and Sima's [19] at small strains and as the numerical cutting force is around 40% smaller than the experiments, the value of A is set to 1936 MPa (the initial value is doubled). The stress–strain evolution of TANH with the modified value of A is called modified TANH in this paper. The increase in the stresses is obvious in Fig. 12, in which it is noted that the curve of the modified TANH model is closer to Karpat's [44] and Sima's [19],

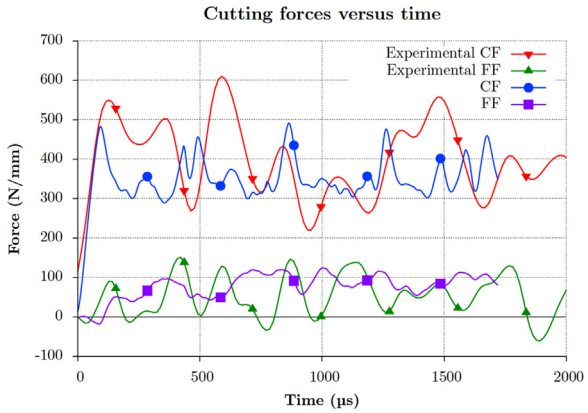

Fig. 14. Cutting forces of the second model at a cutting speed of 30 m/min and a depth of cut of 280 µm, low-pass filter cutoff frequency at 10 kHz.

Table 8
RMS cutting forces comparison; Sim.$_A$ is the model with the modified value of parameter A.

Case	CF (N/mm)	FF (N/mm)
Exp.	386	76
Sim.$_A$	361	86

although the characteristics of each model still lead to distinct evolutions. This alteration of the original value of A is licit since it was originally obtained through inverse analysis by Calamaz et al. [16] for an unknown metallurgical Ti6Al4V state and it brings the stresses level close to this of Karpat's [44] and Sima's [19], which describe the same material.

The modification of the TANH model will result in larger stresses in the workpiece, implying that the separation criterion must be adapted as the tensile failure value used so far will be reached more easily. The objective is to remain consistent with the level modification of the stresses. The value of parameter A has been doubled. As a first guess, it is assumed that the tensile failure value needs also to be doubled to follow this stress increase (the curve in Fig. 9 is translated upwards). The adjustment of the chip separation criterion will be refined in a second time in Section 6.

5.2. Discussion

As shown in Fig. 13, a saw-toothed chip is still formed and Fig. 14 presents the expected increase in the forces. The morphology remains close to the two previous chips. It must, however, be noted that some of the teeth are detaching of the chip due to the appearance of a second crack starting near the tool edge radius. The chip seems to be in one piece because of the presence of some finite elements linking two successive teeth (highlighted by the arrows in Fig. 13). On the first numerical chip (Fig. 10(a)), the valley was nearly two times smaller than the experimental one. This difference has grown with the introduced modifications to the point of leading to a discontinuous chip, as the valley can now be considered equal to zero.

For the forces (Fig. 14) the level is notably improved, as expected. It results in higher RMS values (Table 8) and the difference between the experimental and numerical cutting and feed forces becomes very small. It is similar, even smaller, than the best results in the literature for Ti6Al4V for other cutting conditions: 5–10% for the cutting force and 10–15% for the feed force [18,19,22]. Numerical and experimental forces are cyclic and the magnitude

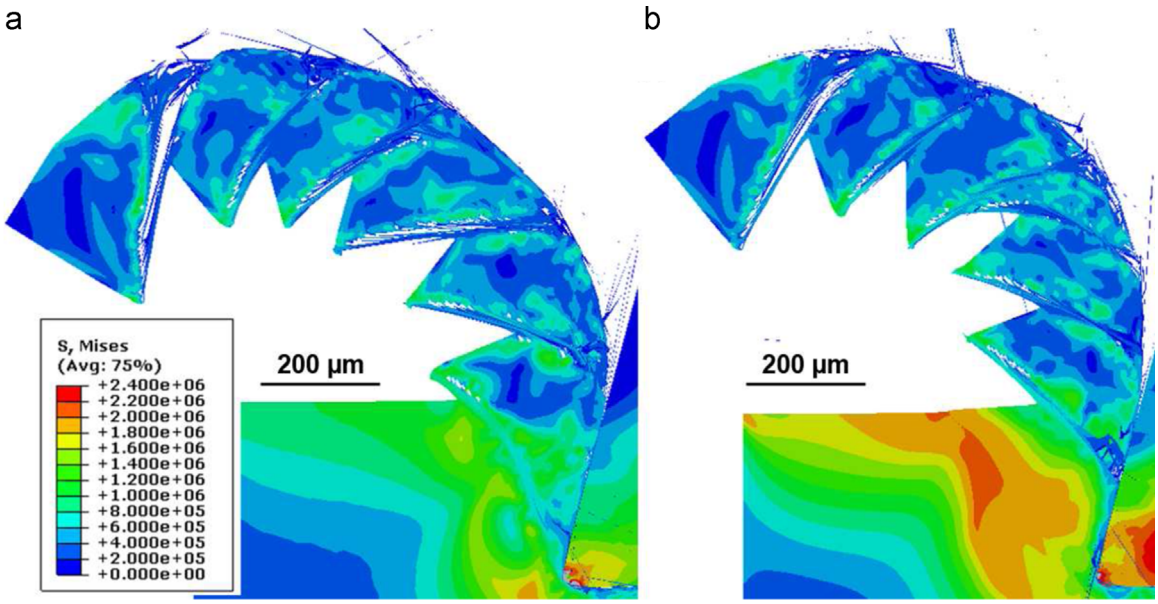

Fig. 15. Chip morphology (Von Mises stresses contours (e^3 Pa)) (a) 10%; (b) 20% model.

of the numerical force variations is closer, though smaller, to that of the experiments. The width of the peaks is still larger for the experimental force. It is due to the teeth, coming off the workpiece. It results in a fast drop in the force and the tool has to move more to be again in contact with the workpiece for the force to rise again. It is also noted that the feed forces are very close to each other (as before) and that the magnitude of the variations is, as well, smaller than experimentally.

The objective of the TANH model modification was to increase the level of the cutting force to bring it close to the experimental one, which has been observed. The morphology is, however, deteriorated and the chip formation mechanism moves away from the experimental one, as a "quasi-discontinuous" chip is formed.

5.3. Conclusions of the influence of the material constitutive model on the results

The modifications of the material constitutive model have a mixed effect on the results. On one side, the quality of the chip morphology is degraded. The problem highlighted with the initial TANH model is amplified: the valley is smaller and a second crack propagates in the primary shear zone from the cutting edge radius of the tool and it ends in the separation of the tooth on the tool side. The crack share in the saw-toothed chip formation is therefore too large. The saw-toothed chip formation of this model moves away from what is experimentally observed.

On the other side, the level of the cutting force is now closer to that measured during the experiments. This augmentation was the objective of the modifications of the material constitutive model. In this sense, it is achieved, as the differences on the forces are now very reduced.

In conclusions, by modifying the material constitutive model and the chip separation criterion in similar proportions, it is mainly the cutting forces that are impacted. The morphology is as well but much less than the efforts. The material constitutive model would therefore mainly acts on the level of the forces. At this point, the chip morphology and formation mechanism should be improved to get closer to the experiments but without dramatically affecting the cutting forces.

6. Influence of the chip separation criterion on the results

6.1. Chip separation criterion modifications

The parameter directly linked to the crack propagation is the chip separation criterion. In the two previous models, the crack propagates too quickly and easily; the damage value should therefore be increased. Modifying the tensile failure value is licit because it is only temperature dependent so far, although high strain rates are encountered during the cut. Strain rate and temperature dependent tensile failure of Ti6Al4V is unfortunately not available in the literature and would not be easily measurable. To take account of the strain rate dependency of tensile failure, it is proposed to pull it up. Two sets (curves) of tensile failure values are suggested: the first is 10% higher than in the previous model and the second is 20% higher.

Fig. 15 presents the chips obtained with the two different values of the chip separation criterion. They are both saw-toothed and similar, with a first valley quite small. In Fig. 15(b), it is clearly seen that, except for the first tooth, there is no crack in the primary shear zone contrary to the experimental chip and the chip of Fig. 15(a). It is deduced that the 20% higher tensile failure values might be too high to represent accurately the Ti6Al4V chip formation. The 10% higher case is therefore adopted.

6.2. Discussion

Micro-cracks are present in the primary shear zone of the third, fourth and fifth teeth without coming out at the free chip surface (Fig. 15(a)), making the measure of the valley not easy. The values presented in Table 9 do not take them into account and the valley obtained this way is therefore an overestimation of the numerical value as no micro-cracks were experimentally observed. The length and the height of the numerical teeth are still lower than those of the experiments.

Like for the initial model and the experiments, the saw-toothed chip formation involves high deformations and crack propagation in the primary shear zone. Similar to the second model (with only the TANH modifications), another crack appears near the cutting edge radius for the second and the fifth teeth. This inconvenience is thus not completely eliminated. A higher value of the chip separation criterion does not solve it, as shown in Fig. 15(b), where

Table 9
Summary of the characteristic lengths of the saw-toothed chips at 280 µm (experiments: 25 teeth, simulation: 4 teeth, σ_x: standard deviation of the length x); $\text{Sim.}_{10\%}$ is the model with 10% higher tensile curve.

Case	L (µm)	σ_L (µm)	C (µm)	σ_C (µm)	H (µm)	σ_H (µm)
Exp.	206	17	157	21	288	14
$\text{Sim.}_{10\%}$	131	18	157	19	275	8

Table 10
RMS cutting forces and teeth formation frequencies comparison; $\text{Sim.}_{10\%}$ is the model with 10% higher tensile curve.

Case	CF (N/mm)	FF (N/mm)	f_g (Hz)	f_f (Hz)	f_s (Hz)
Exp.	386	76	2427	2038	2032
$\text{Sim.}_{10\%}$	378	106	3817	2938	3139

it can be noted that the fifth tooth of this model has also this kind of crack. A noticeable improvement compared to the initial model is the absence of cracks crossing the teeth, in accordance with the experimental chip.

The forces are close to those of the previous model (Table 10) though a bit larger, which was expected as, this time, the teeth are still attached to each other. The cutting force can be considered as identical to the experimental one. The feed force is on the contrary higher than that of the experiments and the difference is larger than for the previous models.

The teeth formation frequency is estimated with the same three methods used for the initial model (cf. Section 4.1). Table 10 summarizes the results. As expected, the frequencies are higher than for the experiments and the initial model. It is mainly due to the teeth being shorter and therefore more quickly formed. It is observed that, experimentally and numerically, the geometry method leads to higher values than these given by the cutting force methods. For the modelings, the best sine in a least squares way results in a frequency higher than with the FFT. Although numerical and experimental frequencies are similar, the differences are not negligible. The teeth formation frequency for the modeling is around 3300 Hz, which is approximately 1000 Hz larger than the experiments and 500 Hz larger than the initial model. The improvements provided on the chip morphology and the cutting force degrades therefore the teeth formation frequency.

6.3. Conclusions of the influence of the chip separation criterion on the results

The chip morphology was qualitatively close to the experiments. The measured lengths were, however, smaller, except for the valley well improved. The drawback of the initial model on this point is no longer relevant. The cracks crossing some teeth of the initial model have disappeared but others appeared in the tool edge radius area for some teeth. The chip formation mechanism was still the conjunction of deformation and crack propagation inside the primary shear zone.

The level of the forces was not much affected by the modification of the level of the chip separation criterion. They were slightly higher than for the previous model, which was expected as a larger valley leads to a wider peak in the force. The RMS value of the cutting force was nearly equal to the experiments. The feed force was on the contrary overestimated by the model.

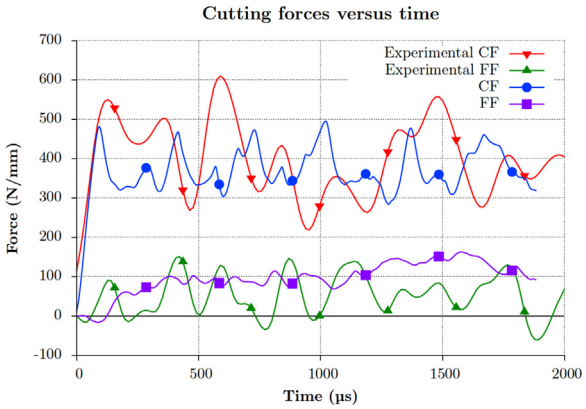

Fig. 16. Cutting forces of the third model at a cutting speed of 30 m/min and a depth of cut of 280 µm, low-pass filter cutoff frequency at 10 kHz.

7. Comparison of the numerical and experimental results at the three other depths of cut

The numerical model will now be used with the three other cutting conditions adopted in the experiments. It means that the same model is adopted but with other cutting conditions. This is consistent with the constraints presented in Section 3 for the development of the model (it should respect the physical phenomena and not influence the chip formation [7]) and its ability to be predictive, which is still not common in the current literature. The modified TANH model and chip separation criterion (cf. Section 6) are considered. The value of the depth of cut is therefore the only difference with the model presented in the previous paragraph.

Fig. 17 shows the modeled chips for the depths of cut of 100 µm (a), 60 µm (b) and 40 µm (c). As for the experiments (Fig. 16(d)–(f)), the chip at 100 µm is not saw-toothed but it is quasi-continuous with small teeth of variable depth. It is the same for the chips at 60 µm and 40 µm; the length of the teeth is smaller. In all three cases, the model produces chips that are globally close to the experiments. The very small teeth observed experimentally at 60 µm and 40 µm are not reproduced by the numerical model, presumably due to the finite elements being larger than these teeth. The chip curl is larger for the numerical chips at 60 µm and 100 µm, indicating that the experimental chip is stiffer. At 40 µm, the experimental and numerical chip curls are close to each other.

The RMS values of the forces for the four depths of cut considered in this work are presented in Table 11 for the cutting forces and in Table 12 for the feed forces. They are compared to the values measured during the experiments.

The modeled cutting force is globally close to the experimental value (difference between 2% and −11%). Except at 280 µm, the numerical feed force is always significantly larger than the measurement: the numerical value is, at least, two times larger than the experimental one. The cutting force decreases with the depth of cut numerically as well as experimentally. The same is observed for the feed force, except at 60 µm, but the decrease is smaller. The cutting force is therefore globally better modeled than the feed force.

Except for the overestimated feed force, the numerical model gives results close to the experiments. The morphology of the chips at various depths of cut is qualitatively close to the observed one. The difference with the RMS value of the cutting force is between 2% and −11%, a value similar to that of the best results from the literature [18,19,22].

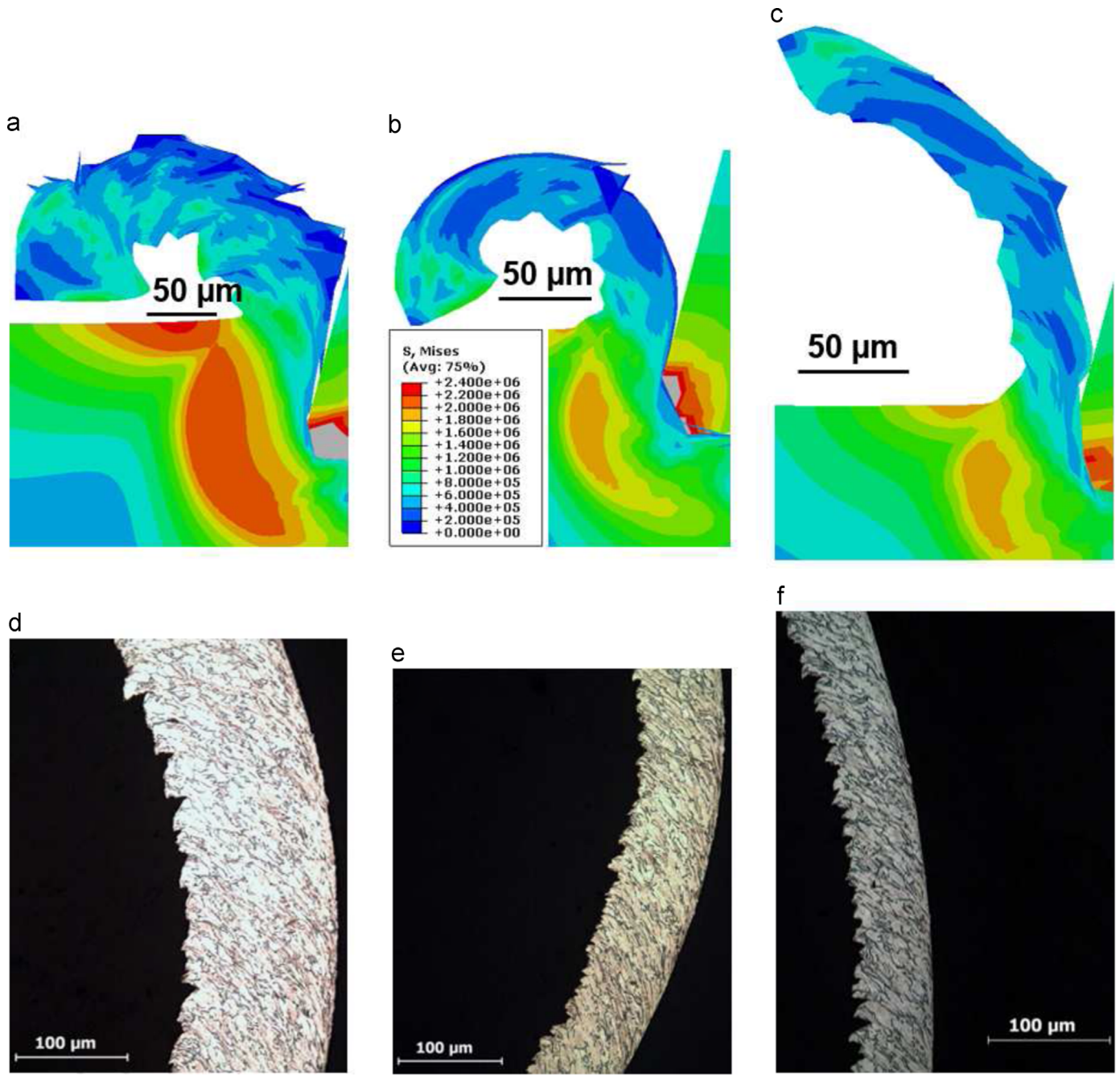

Fig. 17. Chip morphologies (Von Mises stresses contours (e^3 Pa)) and experimental chips [26] at a cutting speed of 30 m/min and a depth of cut of (a, d) 100 µm, (b, e) 60 µm and (c, f) 40 µm (the Von Mises stresses scale is the same for the three depths of cut).

Table 11
RMS cutting forces summary for the four depths of cut.

h (µm)	Exp. (N/mm)	Sim. (N/mm)	Difference (%)
280	386	378	2
100	172	179	−4
60	111	124	−11
40	86	86	0

Table 12
RMS feed forces summary for the four depths of cut.

h (µm)	Exp. (N/mm)	Sim. (N/mm)	Difference (%)
280	76	106	−39
100	50	105	−109
60	44	119	−168
40	41	113	−176

8. Summary of the findings

The experimental setup uses a milling machine in only one cutting direction, as a planning machine. The main advantages of this setup are its universality thanks to the absence of machine modifications; the use of samples with a simple geometry and small dimensions, reducing their machining time and their cost; the certainty to machine in orthogonal cutting conditions and that there is no need for the chip to be unrolled, preventing it from any deformation prior the observation, and the ability to carry out long

(interrupted) machining tests to analyze tool wear. The simplicity of this setup is its greatest strength to enable it to be quickly widespread and used for any material with rather low cutting speeds (compatible with the feed rate of the milling machine).

The experimental results were compared to these of a finite element model, whose material constitutive model and chip separation criterion required to be modified to represent accurately the machined material. This highlighted the partial decoupling between the morphology and the forces (within the limits of the variations considered). Indeed, their level was mainly influenced by the material constitutive model, while the chip separation criterion acted mostly on the chip morphology. It turned out that it was possible to modify one without impacting much the other. The model presented in this paper was not developed for a particular set of cutting conditions but with the aim to respect the physical phenomena and not influence the chip formation. It is therefore predictive, which is still not common in the current literature.

For the cutting conditions adopted in this study, saw-toothed and quasi-continuous chips were formed. When the chip was saw-toothed, the cutting force could be considered as identical to the measured one. The morphology was close to that of the experimental chip and its chip formation mechanism implied the deformation and the crack propagation inside the primary shear zone in both cases. The feed force was on the contrary overestimated. The numerical teeth were shorter, resulting in a higher teeth formation frequency. Micro-cracks were noted in the primary shear zone of the numerical chip; none was observed for the experimental one. When the depth of cut decreased and the chip was no more saw-toothed, the numerical results were still close to the experiments, in terms of morphology and cutting force. The feed force was on the contrary still overestimated, particularly when the depth of cut was low.

The modifications of the material constitutive model were explained by the initial difference between the TANH model and other models from the literature, such as Karpat's [44] or Sima's [19]. Concerning the chip separation criterion, physical meaning must be used as no data are available to compare to the modified criterion.

9. Conclusions

An experimental orthogonal cutting benchmark has been introduced to validate finite element models. The comparison with the modeling showed that the influence of the constitutive model and the chip separation criterion on the results is nearly decoupled. The cutting forces are mainly influenced by the constitutive model while the chip morphology is mainly controlled by the chip separation criterion. For chip morphologies ranging from saw-toothed to continuous, the numerical results were close to the experimental reference without further change in the model and the chips formation mechanisms were close. Future work should focus on the development of a new experimental setup to measure the evolution of Ti6Al4V tensile failure versus temperature (as currently) but also versus strain rate. This information on the shear would also be needed to improve the modeling as the material is highly sheared during the cut. The adoption of other material constitutive models such as Karpat's [44] or Sima's [19] should also be carried out to study their influence on the cutting forces and the chip morphology.

Acknowledgments

The authors gratefully acknowledge TechnoCampus for making their experimental resources available to us; the Metallurgy Department of the UMONS Faculty of Engineering for making their microstructure analysis resources available to us; and Prof. P. Lambert from the *Université Libre de Bruxelles* for the high speed camera.

References

[1] The French Titanium Association, ⟨http://www.titane.asso.fr/markets-and-applications.html⟩. The French Titanium Association: Markets and applications, 2013-09-13; 2011.
[2] Destefani J. Introduction to titanium and titanium alloys, properties and selection: nonferrous alloys and special-purpose materials, ASM Handbook, vol. 2, 1990.
[3] Combres Y. Propriétés du titane et de ses alliages, Editions T.I., 2013.
[4] Combres Y, Champin B. Traitements thermiques des alliages de titane, Editions T.I, 2013.
[5] The ASM Handbook Committee, Fatigue and fracture properties of titanium alloys, vol. 2, 10th edition. ASM International; 1997.
[6] Ezugwu E, Wang Z. Titanium alloys and their machinability—a review. J Mater Process Technol 1997;68:262–74.
[7] Ducobu F, Rivière-Lorphèvre E, Filippi E. Numerical contribution to the comprehension of saw-toothed Ti6Al4V chip formation in orthogonal cutting. Int J Mech Sci 2014;81:77–87.
[8] Molinari A, Musquar C, Sutter G. Adiabatic shear banding in high speed machining of Ti–6Al–4V: experiments and modeling. Int J Plast 2002;18:443–59.
[9] Owen D, Vaz M. Computational techniques applied to high-speed machining under adiabatic strain localization conditions. Comput Methods Appl Mech Eng 1999;171:445–61.
[10] Fourment L, Delalondre F. A 3D study of the influence of friction on the adiabatic shear band formation during high speed machining. In: Proceedings of the ESAFORM2008 conference, 2008.
[11] Bäker M, Rosler J, Siemers C. A finite element model of high speed metal cutting with adiabatic shearing. Comput Struct 2002;80:495–513.
[12] Komanduri R. Some clarifications on the mechanics of chip formation when machining titanium alloys. Wear 1982;76:15–34.
[13] Vyas A, Shaw MC. Mechanics of saw-tooth chip formation in metal cutting. J Manuf Sci Eng 1999;121:163–72.
[14] Hua J, Shivpuri R. Prediction of chip morphology and segmentation during the machining of titanium alloys. J Mater Process Technol 2004;150:124–33.
[15] Bai Y, Dodd B. Adiabatic shear localisation: occurrence, theories and applications. Oxford: Pergamon Press; 1992.
[16] Calamaz M, Coupard D, Girot F. A new material model for 2D numerical simulation of serrated chip formation when machining titanium alloy Ti–6Al–4V. Int J Mach Tools Manuf 2008;48:275–88.
[17] Umbrello D. Finite element simulation of conventional and high speed machining of Ti6Al4V alloy. J Mater Process Technol 2008;196:79–87.
[18] Karpat Y. Temperature dependent flow softening of titanium alloy Ti6Al4V: an investigation using finite element simulation of machining. J Mater Process Technol 2011;211:737–49.
[19] Sima M, Özel T. Modified material constitutive models for serrated chip formation simulations and experimental validation in machining of titanium alloy Ti–6Al–4V. Int J Mach Tools Manuf 2010;50:943–60.
[20] Mabrouki T, Girardin F, Asad M, Rigal J-F. Numerical and experimental study of dry cutting for an aeronautic aluminium alloy (A2024-T351). Int J Mach Tools Manuf 2008;48:1187–97.
[21] Zhang Y, Mabrouki T, Nelias D, Gong Y. FE-model for titanium alloy (Ti–6Al–4V) cutting based on the identification of limiting shear stress at tool-chip interface. Int J Mater Form 2011;4:11–23.
[22] Zhang Y, Mabrouki T, Nelias D, Gong Y. Chip formation in orthogonal cutting considering interface limiting shear stress and damage evolution based on fracture energy approach. Finite Elem Anal Des 2011;47:850–63.
[23] Wan Z, Zhu Y, Liu H, Tang Y. Microstructure evolution of adiabatic shear bands and mechanisms of saw-tooth chip formation in machining Ti6Al4V. Mater Sci Eng A 2012;531:155–63.
[24] Barry J, Byrne G. The mechanisms of chip formation in machining hardened steels. J Manuf Sci Eng 2002;124:528–35.
[25] Wang B, Liu Z. Serrated chip formation mechanism based on mixed mode of ductile fracture and adiabatic shear. Proc Inst Mech Eng Part B: J Eng Manuf 2013;228:181–90.
[26] Ducobu F, Rivière-Lorphèvre E, Filippi E. Experimental contribution to the study of the Ti6Al4V chip formation in orthogonal cutting on a milling machine. Int J Mater Form 2015;8:455–68.
[27] Altintas Y. Manufacturing automation: metal cutting mechanics, machine tool vibrations, and CNC design. Cambridge: Cambridge University Press; 2012.
[28] Mahnama M, Movahhedy M. Prediction of machining chatter based on FEM simulation of chip formation under dynamic conditions. Int J Mach Tools Manuf 2010;50:611–20.

[29] Filice L, Micari F, Rizzuti S, Umbrello D. Dependence of machining simulation effectiveness on material and friction modelling. Mach Sci Technol: An Int J 2008;12:370–89.
[30] Lampman S. Wrought Titanium and titanium alloys, properties and selection: nonferrous alloys and special-purpose materials, vol. 2. ASM Handbook, 1990.
[31] Pantalé O, Bacaria J-L, Dalverny O, Rakotomalala R, Caperaa S. 2D and 3D numerical models of metal cutting with damage effects. Comput Methods Appl Mech Eng 2004;193:4383–99.
[32] Ducobu F, Rivière-Lorphèvre E, Filippi E. A Lagrangian FEM model to produce saw-toothed macro-chip and to study the depth of cut influence on its formation in orthogonal cutting of Ti6Al4V. Adv Mater Res 2011;223:3–11.
[33] Ducobu F, Rivière-Lorphèvre E, Filippi E. Chip formation in micro-cutting. J Mech Eng Autom 2013;3:441–8.
[34] SECO TOOLS, Turning catalog and technical guide 2012, Organization SECO TOOLS AB, 2011.
[35] Sun S, Brandt M, Dargusch M. Characteristics of cutting forces and chip formation in machining of titanium alloys. Int J Mach Tools Manuf 2009;49:561–8.
[36] Johnson G, Cook W. A constitutive model and data for metals subjected to large strains, high strain rates and high temperatures. In: Proceedings of the seventh international symposium on ballistics, The Hague, The Netherlands, 1983. p. 541–7.
[37] Ding R, Guo Z, Wilson A. Microstructural evolution of a Ti–6Al–4V alloy during thermomechanical processing. Mater Sci Eng A 2002;327:233–45.
[38] Özel T, Zeren E. Numerical modelling of meso-scale finish machining with finite edge radius tools. Int J Mach Mach Mater 2007;2:451–768.
[39] Sun J, Guo YB. Material flow stress and failure in multiscale machining titanium alloy Ti–6Al–4V. Int J Adv Manuf Technol 2009;41:651–9.
[40] Nasr M, Ng EG, Elbestawi M. Effects of workpiece thermal properties on machining-induced residual stresses – thermal softening and conductivity. Proc Inst Mech Eng Part B: J Eng Manuf 2007;221:1387–400.
[41] Woon K, Rahman M, Fang F, Neo K, Liu K. Investigations of tool edge radius effect in micromachining: a FEM simulation approach. J Mater Process Technol 2007;167:316–37.
[42] Meyer HW, Kleponis DS. Modeling the high strain rate behavior of titanium undergoing ballistic impact and penetration. Int J Impact Eng 2001;26:509–21.
[43] Calamaz M, Coupard D, Nouari M, Girot F. Numerical analysis of chip formation and shear localisation processes in machining the Ti–6Al–4V titanium alloy. Int J Adv Manuf Technol 2011;52:887–95.
[44] Karpat Y. Finite element modeling of machining titanium alloy Ti-6Al-4V using a modified material model. In: Proceedings of the 12th CIRP conference on modeling of machining operations, 2009. p. 107–14.